

Supplementary Information for:

Suppression of thermal conductivity without impeding electron mobility in n-type XNiSn half-Heusler thermoelectrics

S.A. Barczak,¹ R.J. Quinn,¹ J.E. Halpin,² K. Domosud,³ R.I. Smith,⁴ A. R. Baker,⁵ E. Don,⁶ I. Forbes,⁷ K. Refson,³ D.A. MacLaren^{2*} and J.W.G. Bos^{1*}

¹ *Institute of Chemical Sciences and Centre for Advanced Energy Storage and Recovery, School of Engineering and Physical Sciences, Heriot-Watt University, Edinburgh, EH14 4AS, UK.*

² *SUPA, School of Physics and Astronomy, University of Glasgow, Glasgow G12 8QQ, UK*

³ *Department of Physics, Royal Holloway University London, Egham, TW20 0EX, UK*

⁴ *ISIS Facility, Rutherford Appleton Laboratory, Harwell Oxford, Didcot OX11 0QX, UK*

⁵ *Diamond Light Source, Harwell Campus, Didcot, Oxfordshire, OX11 0DE, UK*

⁶ *SemiMetrics Ltd., Kings Langley WD4 9WB, UK*

⁷ *Department of Physics and Engineering, Northumbria University, Newcastle NE1 8ST, UK*

* dmaclaren@physics.org; * j.w.g.bos@hw.ac.uk

Single Parabolic Band modelling

The Single Parabolic Band (SPB) model has been widely used to analyse the electrical properties of thermoelectric materials and our analysis closely follows published work on half-Heuslers.^{1,2} The model is described in terms of Fermi integrals, which for the case of acoustic phonon dominated electrical transport are given as:

$$F_i(\eta) = \int_0^{\infty} \frac{\varepsilon^i}{1 + \exp[\varepsilon - \eta]} d\varepsilon \quad (S1)$$

Here ε and η are the reduced energy and Fermi level, respectively, and i is the index of the function. The parabolic band is characterised by a density of states effective mass (m_{DoS}^*), which is obtained by fitting a Pisarenko plot of $|S|$ vs n_H . In the SPB model S and n_H are given by:

$$S = \frac{k_B}{e} \left(\frac{2F_1}{F_0} - \eta \right); \quad (S2)$$

$$n_H = \frac{8\pi}{3} \left(\frac{2m_{DoS}^* k_B T}{h^2} \right)^{3/2} \frac{2F_0^2}{F_{-0.5}}. \quad (S3)$$

For the experimental data shown in Figure 6b in the main article, the best-fit value of m_{DoS}^* is $4.1m_e$. Analysis of the experimental Hall (μ_H) mobility uses the following relation:

$$\mu_H = \left(\frac{F_{-0.5}}{2F_0} \right) \mu_0. \quad (S4)$$

Here μ_0 contains the material specific electron scattering channels, which are summed according to Matthiessen's rule and in our model include acoustic phonon scattering (μ_0^{ph}), X-site alloy scattering ($\mu_0^{al,X}$) and interstitial Cu alloy scattering ($\mu_0^{al,Cu}$):

$$\mu_0^{ph} = \frac{\pi e \hbar^4}{\sqrt{2} (k_B T)^{3/2} E_{def}^2} \frac{v_L^2 d}{m_b^* m_I^*}; \quad (S5)$$

$$\mu_0^{al,X} = \frac{8e \hbar^4}{3\sqrt{2} (k_B T)^{1/2} E_{al}^2 x(1-x)} \frac{N_0}{m_b^* m_I^*}; \quad (S6)$$

$$\mu_0^{al,Cu} = \frac{8e\hbar^4}{3\sqrt{2}(k_B T)} \frac{N_0}{^{1/2}E_{al}^2 y(1-y)} \frac{1}{m_b^*{}^{3/2} m_I^*}. \quad (S7)$$

The strength of the acoustic phonon interaction is characterised by a deformation potential E_{def} , which is set to 5 eV based on the literature,¹ while the alloy deformation potential ($E_{\text{al}} = 0.2$ eV) was used as a fitting parameter. Since the X-site composition does not change for our samples, the alloy fraction x was kept fixed. The other parameters are the velocity of sound $v_L = 3600$ m s⁻¹, the density of the sample, d , the number of atoms per unit volume, N_0 , while the band mass m_b^* can be obtained from $m_{DoS}^* = N_v^{2/3} m_b^*$, where $N_v = 3$ is the conduction band degeneracy and we have assumed isotropic transport and set $m_b^* = m_I^*$.

Once the energy dependence (n_H) of S and μ_H are established ZT can be calculated using:

$$ZT = \frac{S^2 \sigma}{L \sigma T + \kappa_l} T \quad (S8)$$

with the Lorenz number (L) and electrical conductivity (σ) given by:

$$L = \frac{k_B^2 3F_0 F_2 - 4F_1^2}{e^2 F_0^2}; \quad (S9)$$

$$\sigma = n_H e \mu_H. \quad (S10)$$

Table S1: Lattice parameters (a), weight percentage (wt%), volume percentage (v%), fractional site occupancies (occ), thermal displacement parameters ($U_{\text{iso}}/\text{\AA}^2$) and refined compositions for the half-Heusler and Ni_3Sn_2 phases that were used to fit the Polaris neutron powder diffraction data collected for $\text{Ti}_{0.5}\text{Zr}_{0.25}\text{Hf}_{0.25}\text{NiCu}_y\text{Sn}$ materials.

	y = 0.025	y = 0.05	y = 0.075
Half-Heusler Phase			
a (Å)	6.01528(8)	6.01617(6)	6.02732(5)
wt%	99.3(1)	98.5(1)	100
Ti/Zr/Hf Occ	0.515(3) / 0.242(1) / 0.242(1)	0.516(3) / 0.242(1) / 0.242(1)	0.493(6) / 0.246(3) / 0.246(3)
(4a) U_{iso}	0.0011(5)	0.0030(5)	0.0054(4)
Ni (4c) U_{iso}	0.0050(1)	0.0053(1)	0.0056(1)
Cu (4d) Occ	0.041(2)	0.049(2)	0.073(2)
U_{iso}	0.0050(1)	0.0053(1)	0.0056(1)
Sn (4b) U_{iso}	0.0071(4)	0.0058(4)	0.0046(2)
Refined composition	$\text{Ti}_{0.515(3)}\text{Zr}_{0.242(1)}\text{Hf}_{0.242(1)}\text{Ni}_{1.00}\text{Cu}_{0.041(2)}\text{Sn}$	$\text{Ti}_{0.516(3)}\text{Zr}_{0.242(1)}\text{Hf}_{0.242(1)}\text{Ni}_{1.00}\text{Cu}_{0.049(2)}\text{Sn}$	$\text{Ti}_{0.493(6)}\text{Zr}_{0.246(3)}\text{Hf}_{0.246(3)}\text{NiCu}_{0.073(2)}\text{Sn}$
ρ_{HH} (g cm⁻³)	8.241	8.378	8.252
Ni₃Sn₂ Phase			
a (Å)	4.0976(8)	4.1161(5)	
c (Å)	5.131(1)	5.1236(9)	
v (Å ³)	74.61(2)	75.18(1)	
wt%	0.7(1)	1.5(1)	
Ni (2a) U_{iso}	0.008(2)	0.008(1)	
Ni (2d) U_{iso}	0.008(2)	0.008(1)	
Sn (2c) U_{iso}	0.008(2)	0.008(1)	
ρ (g cm⁻³)	9.203	8.163	
Fit Statistics			
χ^2 (Rietveld) / χ^2 (Le Bail)	1.00	0.98	0.93
wR_p (%) bank 3	3.16	2.97	2.96
bank 4	2.47	2.21	2.29
bank 5	2.43	2.08	1.99
R_p (%) bank 3	3.26	3.24	3.05
bank 4	4.22	4.40	3.41
bank 5	3.54	3.11	2.90
Average composition	$\text{Ti}_{0.5}\text{Zr}_{0.235}\text{Hf}_{0.235}\text{Ni}_{1.018}\text{Cu}_{0.040}\text{Sn}_{0.983}$	$\text{Ti}_{0.5}\text{Zr}_{0.234}\text{Hf}_{0.234}\text{Ni}_{1.013}\text{Cu}_{0.045}\text{Sn}_{0.998}$	$\text{Ti}_{0.493(6)}\text{Zr}_{0.246(3)}\text{Hf}_{0.246(3)}\text{NiCu}_{0.073}\text{Sn}$

Table S2. Room temperature Seebeck coefficient (S), electrical resistivity (ρ), lattice thermal conductivity (κ_{lat}), figure of merit (ZT), Hall carrier concentrations (n_H), Hall mobilities (μ_H) and electrical resistivity (ρ_H) from the Hall disks for the $Ti_{0.5}Zr_{0.25}Hf_{0.25}NiCu_ySn$ series.

y	S (μVK^{-1})	ρ ($m\Omega cm$)	κ_{lat} ($Wm^{-1}K^{-1}$)	ZT	n_H ($10^{20} cm^{-3}$)	μ_H ($cm^2V^{-1}s^{-1}$)	ρ_H ($m\Omega cm$)
0	-219 (± 11)	4.788 (± 0.239)	3.07 (± 0.31)	0.11	1.243 (± 0.06)	12.687 (± 0.63)	3.958 (± 0.198)
0.0125	-156 (± 8)	1.051 (± 0.053)	--	--	2.643 (± 0.13)	22.075 (± 1.10)	1.070 (± 0.053)
0.025	-126 (± 6)	0.716 (± 0.036)	2.82 (± 0.28)	0.20	4.704 (± 0.24)	21.275 (± 1.06)	0.623 (± 0.031)
0.0375	-105 (± 5)	0.537 (± 0.027)	--	--	6.311 (± 0.32)	18.787 (± 0.94)	0.526 (± 0.026)
0.05	-91 (± 5)	0.489 (± 0.024)	2.65 (± 0.27)	0.15	8.436 (± 0.42)	17.552 (± 0.88)	0.422 (± 0.021)
0.075	-73 (± 4)	0.354 (± 0.018)	2.66 (± 0.27)	0.11	13.62 (± 0.68)	15.432 (± 0.77)	0.298 (± 0.015)

Table S3: Lattice thermal conductivities ($\text{W m}^{-1} \text{K}^{-1}$) for XNiCu_ySn half-Heusler end-members with $y = 0$ and $y = 0.075$ ($X = \text{Ti}, \text{Zr}$ and Hf).³

y	X = Ti	X = Zr	X = Hf
0	6.1	9.2	6.7
0.075	3.9	5.9	6.1

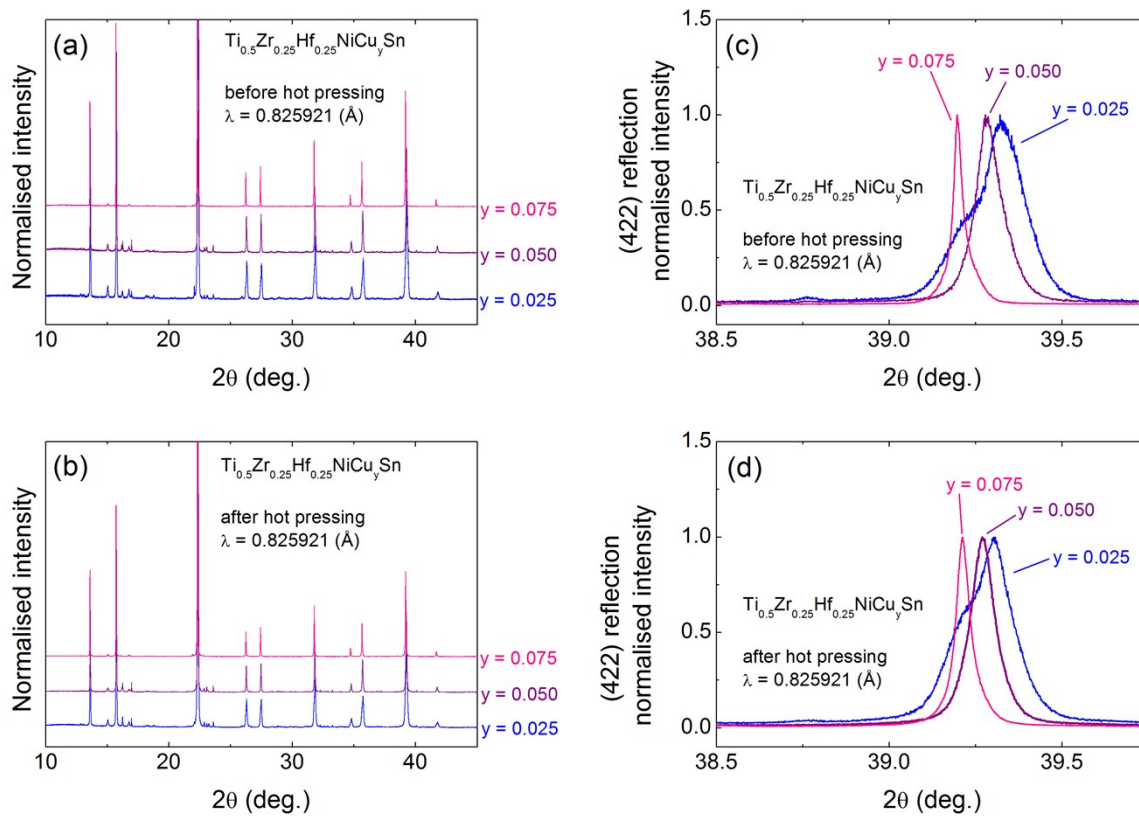


Figure S1: Comparison of synchrotron X-ray powder diffraction data for the $\text{Ti}_{0.5}\text{Zr}_{0.25}\text{Hf}_{0.25}\text{NiCu}_y\text{Sn}$ series before **(a, c)** and after **(b, d)** hot pressing. Sample consolidation has little impact on the peak shape of the (422) reflection, suggesting that the half-Heusler phase distribution, primarily due to the poor mixing of the X-metals, does not change significantly.

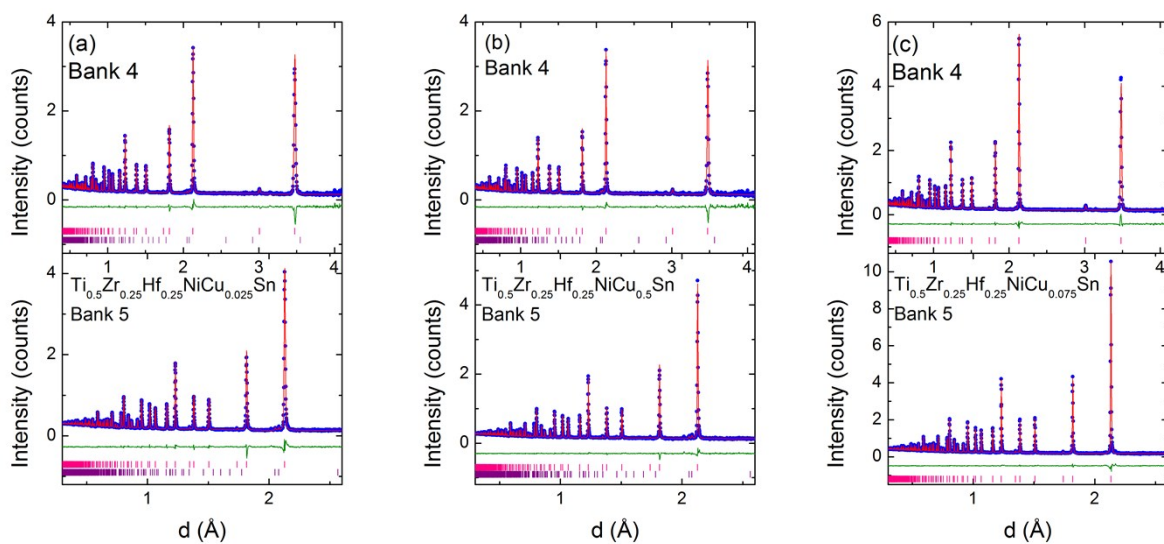


Figure S2: Rietveld refinements of Polaris neutron powder diffraction data for selected $\text{Ti}_{0.5}\text{Zr}_{0.25}\text{Hf}_{0.25}\text{NiCu}_y\text{Sn}$ half-Heusler compositions. Blue circles are the observed data, red lines are the calculated intensities and green lines are difference curves. Pink (top row) reflection markers are for the half-Heusler phase, purple markers (bottom row) are for Ni_3Sn_2 .

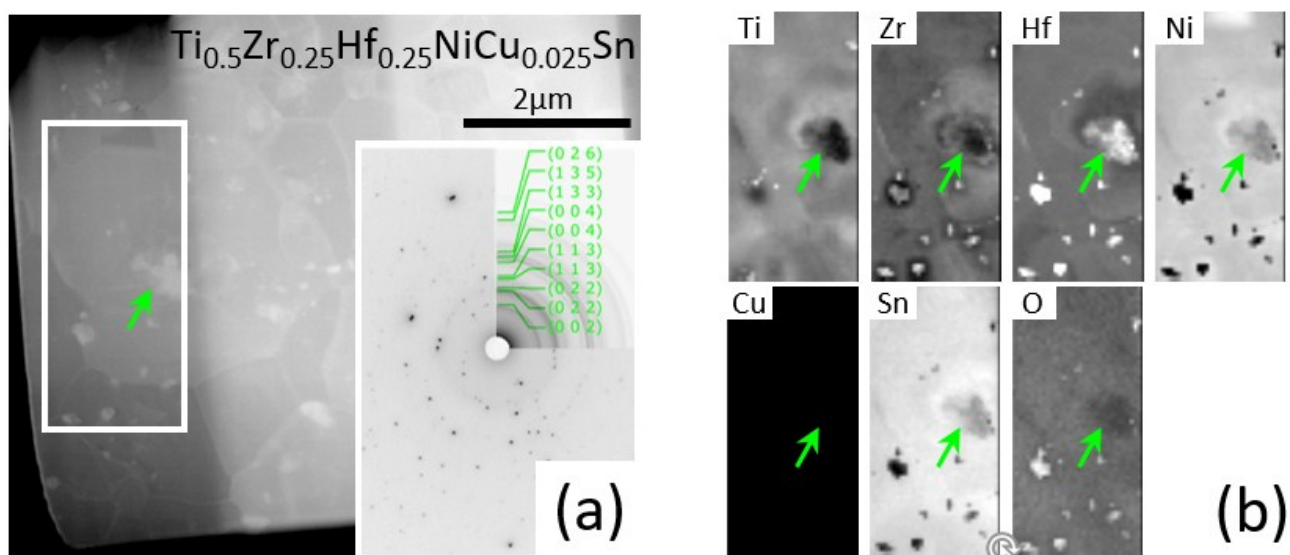


Figure S3: STEM analysis of phase segregation in the $\text{Ti}_{0.5}\text{Zr}_{0.25}\text{Hf}_{0.25}\text{NiCu}_{0.025}\text{Sn}$ sample. (a) In dark-field HAADF STEM, regions with a higher atomic number appear brighter. The lamella has been taken from the centre of the sample and thinned using focused ion beam techniques in a series of steps, the thinnest being on the left of the image, with (inset) a selected area diffraction pattern with radial average indexed to HH diffraction conditions. Elemental mapping has been performed for the area in the white box using STEM-EELS, which straddles a grain that can be discerned in the contrast variations of the STEM image. Elemental maps are presented in (b) and derive from background-subtracted, deconvolved spectra, using the K-edge for O, the $L_{2,3}$ edges for Ti, Ni and Zr and the $M_{4,5}$ edges for Sn and Hf. A Hf rich grain ‘seed’ is indicated by the green arrow whilst other bright spots in the Hf map correlate with oxygen intensity and so indicate a minority presence of hafnium oxides located at the grain boundaries. The Hf ‘seed’ has previously been seen in Ref (17), where it is suggested that grains nucleate on Hf inclusions since the high melting point of Hf leads it to solidify early in the cooling process. Surrounding the Hf rich seed, variation in the HH composition can be seen with the grain being richer in Zr towards the centre and with Ti-rich regions dominating the bulk of the grain. Copper is difficult to detect at this atomic concentration. This coherent formation of the grain around the Hf seed during cooling, explains the ‘core-shell’ type structure seen in by EBSD/EDS.

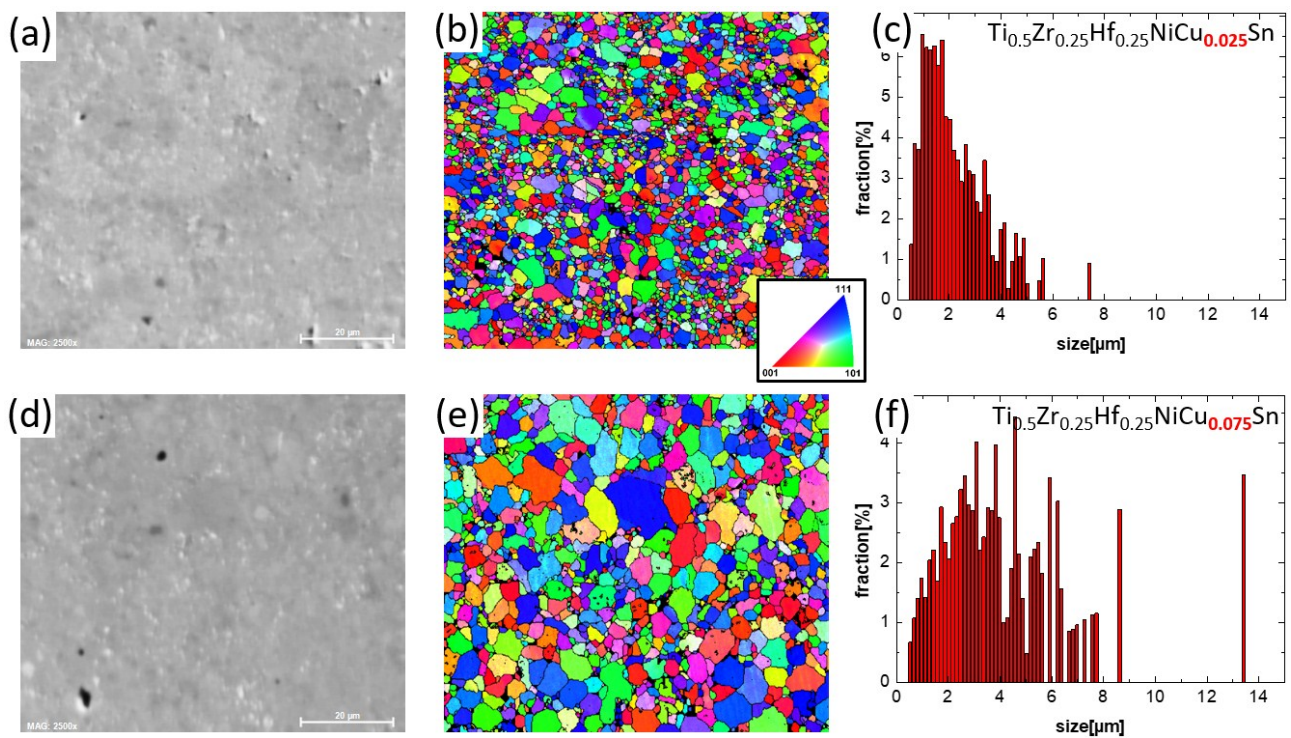


Figure S4: Granularity analysis of (a–c) $\text{Ti}_{0.5}\text{Zr}_{0.25}\text{Hf}_{0.25}\text{NiCu}_{0.025}\text{Sn}$ and (d–f) $\text{Ti}_{0.5}\text{Zr}_{0.25}\text{Hf}_{0.25}\text{NiCu}_{0.075}\text{Sn}$ samples showing (left) scanning electron microscopy images, (middle) electron backscatter diffraction (EBSD) maps that are coloured according to their crystallographic orientation (ie. an inverse pole figure – see key for orientation) and (right) the measured area fraction weighted grain size. There is a clear increase in grain size with addition of Cu.

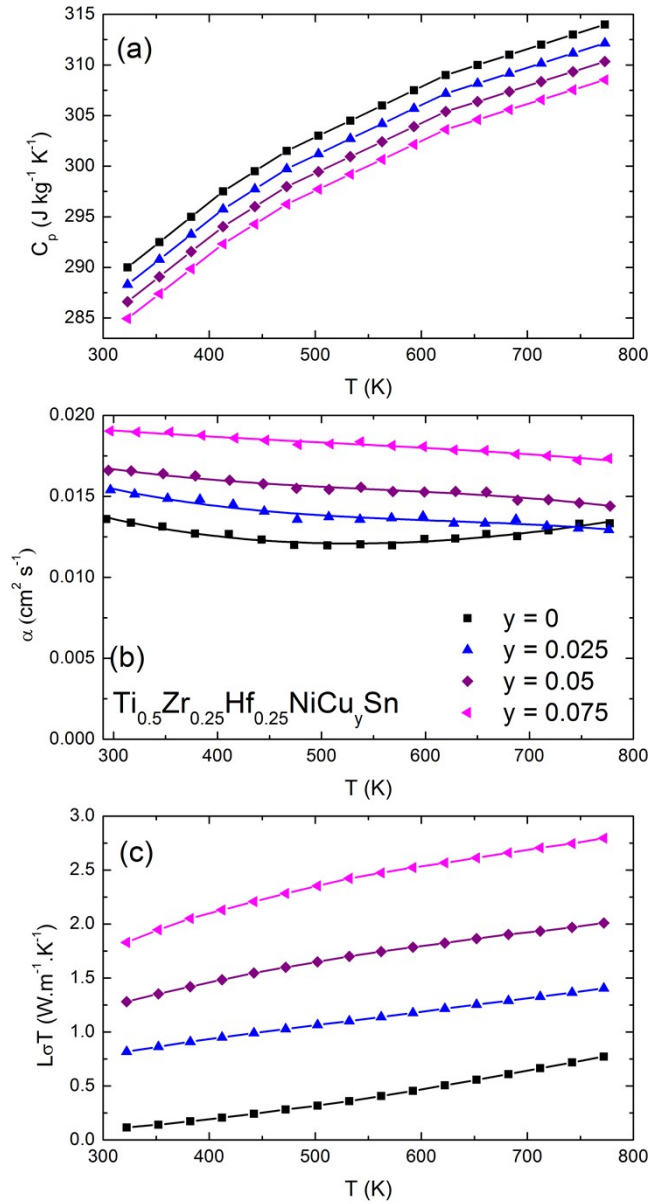


Figure S5: Temperature dependence of (a) the heat capacity (C_p), where the values for $y > 0$ were estimated using a molar mass correction, (b) the thermal diffusivity (α) and (c) the electronic thermal conductivity, $\kappa_{el} = LT/\rho$, where the Lorenz number, L , was obtained using the empirical expression derived in Ref. 4.

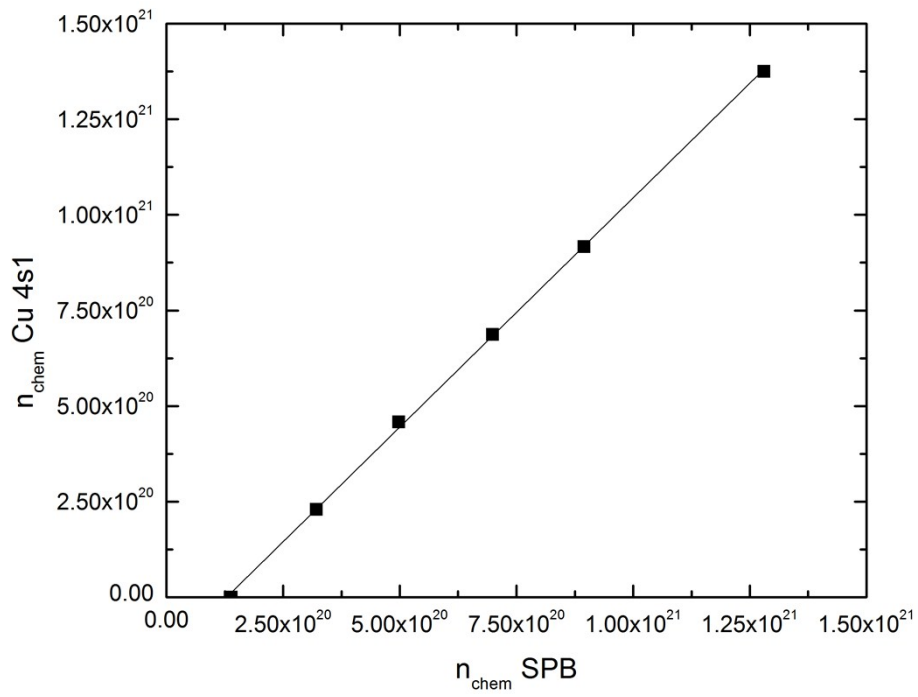


Figure S6: Correlation between the chemical carrier concentration ($n_{Chem} \text{ Cu}4s^1$), calculated from the experimental unit cell volumes and donation of a single $4s^1$ electron / Cu, and the chemical carrier concentration ($n_{chem} \text{ SPB}$), calculated from n_H by considering the Hall factor, for the $\text{Ti}_{0.5}\text{Zr}_{0.25}\text{Hf}_{0.25}\text{NiCu}_y\text{Sn}$ half-Heuslers.

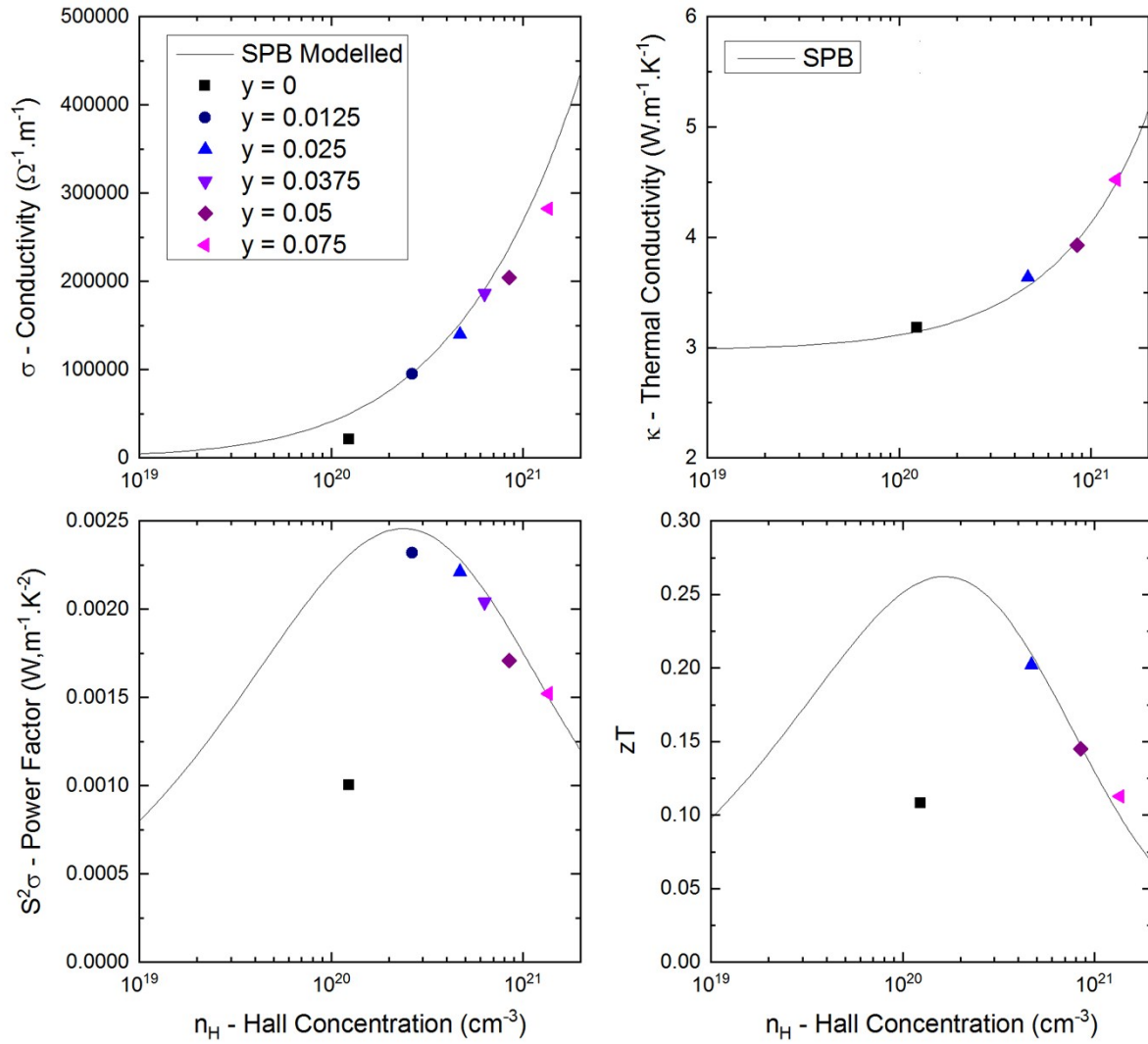


Figure S7: Evolution of **(a)** the room temperature electrical conductivity ($\sigma = 1/\rho$), **(b)** total thermal conductivity ($\kappa = \kappa_{lat} + L\sigma T$) and **(c)** power factor ($S^2\sigma$) and **(d)** the figure of merit ZT for the $\text{Ti}_{0.5}\text{Zr}_{0.25}\text{Hf}_{0.25}\text{NiCu}_y\text{Sn}$ samples. Solid lines are calculated trends from the single parabolic band model. Here, κ_{lat} was assumed to reduce linearly with n_H , leading to excellent agreement with the measured κ values, providing further evidence that interstitial Cu is an effective phonon scattering centre.

References

1. H. H. Xie, H. Wang, Y. Z. Pei, C. G. Fu, X. H. Liu, G. J. Snyder, X. B. Zhao and T. J. Zhu, *Advanced Functional Materials*, 2013, **23**, 5123-5130.
2. Y. T. Liu, H. H. Xie, C. G. Fu, G. J. Snyder, X. B. Zhao and T. J. Zhu, *Journal of Materials Chemistry A*, 2015, **3**, 22716-22722.
3. S. A. Barczak, PhD, Heriot-Watt University, 2018.
4. H. S. Kim, Z. M. Gibbs, Y. L. Tang, H. Wang and G. J. Snyder, *APL Mater.*, 2015, **3**, 041506.